RSC Advances

PAPER

Check for updates

Cite this: *RSC Adv.*, 2023, **13**, 344

Study of the denitration performance of a ceramic filter using a manganese-based catalyst

Zhenzhen Wang, [ID] [ab] Shuchuan Peng,[a] Chengzhu Zhu, [ID] [a] Bin Wang,[c] Bo Du,[a] Ting Cheng, [ID] [a] Zhaozhong Jiang[a] and Lei Sun [ID] *[b]

A MnO$_x$/γ-Al$_2$O$_3$ catalyst was prepared by impregnation of manganese acetate and alumina. After optimizing the composition, it was loaded into a ceramic filter (CF) by a one-step coating method. The results show that MnO$_x$/γ-Al$_2$O$_3$ had the best denitration activity when the Mn loading was 4 wt% with a calcination temperature of 400 °C. The MnO$_x$/γ-Al$_2$O$_3$ catalyst ceramic filter (MA-CCF) was made by loading the CF twice with MnO$_x$/γ-Al$_2$O$_3$. When face velocity (FV) was 1 m min^{-1}, MA-CCF displayed more than 80% NO conversion at 125–375 °C and possessed a good resistance of H$_2$O and SO$_2$. The abundant surface adsorbed oxygen, dense membrane and high-density fiber structure on the outer layer of CF effectively protected the catalyst and could improve MA-CCF denitration activity. The multiple advantages of MA-CCF made it possible for good application prospects.

1 Introduction

The glass industry is an important industry related to economic development and people's life, but the emission of furnace flue gas seriously affects the atmospheric environment. The outlet temperature of glass furnace flue gas is 450–550 °C, and the temperature after waste heat recovery is about 150–300 °C. While the NO$_x$ concentration of glass furnaces fueled by natural gas is 1800–2870 mg m^{-3}, the SO$_2$ concentration is 100–500 mg m^{-3}, and the particulate matter concentration is 80–280 mg m^{-3}, respectively.[1–3] At present, the flue gas treatment system widely used in industrial kilns is a tandem technique composed of a dust collector, desulfurization equipment and SCR. But it requires complex processes, large floor space, and high investment.[4,5] Compared with the traditional technique, a catalyst ceramic filter (CCF) has an advantageous corrosion tolerance, high-temperature tolerance and does not need production to be stopped when it is replaced. Its dense external film and internal fiber can remove 99% of the dust in the flue gas, and the internally loaded catalyst can react with NO$_x$ in the gas flow to decompose it into N$_2$ and H$_2$O. Due to its ability to synchronize the dust removal and denitration of the exhaust gas in a set of devices, the CCF has great application prospects in the glass industry.

Choi *et al.*[6–8] developed a V$_2$O$_5$–WO$_3$/TiO$_2$-based CCF with good high-temperature tolerance by a coating process applying

[a]School of Resource and Environmental Engineering, Hefei University of Technology, Hefei, 230009, China

[b]Anhui Academy for Ecological and Environmental Science Research, Hefei, 230071, China. E-mail: sunlei551@qq.com

[c]CNBM Environmental Protection Research Institute(Jiangsu)Co., Ltd., Yancheng, 224051, China

centrifugal force. The NO conversion was more than 95% at 320 °C. Heidenreich *et al.*[9,10] studied the pilot tests of a V$_2$O$_5$–WO$_3$/TiO$_2$-based CCF in a 3.5 WM$_{th}$ biomass combustion plant, and showed that the denitration conversion reached 83.3ϖ% (NH$_3$: NO = 0.87) under the working conditions of 300 °C and face velocity (FV) of 2.5 cm s^{-1}. An *et al.*[11] used the sol–gel method to load the TiO$_2$ on the ceramic filter and then loaded V$_2$O$_5$ to prepare V$_2$O$_5$–TiO$_2$ CCF, and NO conversion reached about 80% at 350 °C. Yu *et al.*[12] prepared V$_2$O$_5$–WO$_3$–MoO$_3$/TiO$_2$ catalytic filter by coating method, and the denitrification efficiency was greater than 90% at 220–380 °C. Their experiments found that catalysts with high vanadium content had more active sites, the agglomeration of particles was more severe at high temperatures. The strong adsorption capacity of agglomerated particles led to the increase of ammonia nitrogen content, which led to the decrease of catalyst selectivity. Zhang *et al.*[13] studied cordierite catalytic filters by one-step and two-step processes and found the one-step process promoted catalyst dispersion in cordierite and had better N$_2$ selectivity. Generally, the catalyst loaded on the CF is V$_2$O$_5$–WO$_3$/TiO$_2$, it is expensive, its operating temperature window is high and narrow (300–400 °C). The melting and volatilization of vanadium release toxic gases, causing secondary pollution. The potential task for applying the CCF in the industry with low flue gas temperature (150–300 °C) is how to widen temperature window by replacing the catalyst.[13–16]

Mn-based catalyst has become the research focus of SCR catalyst due to wider temperature windows and variable valence states.[17,18] Zhou *et al.*[19] discovered MnO$_x$/α-Fe$_2$O$_3$ achieved over 90% NO conversion at 200–350 °C. Wang *et al.*[20] found that the formation of amorphous MnO$_x$ had better SCR performance and good resistance to SO$_2$ and H$_2$O. γ-Al$_2$O$_3$ is often used as

support catalytic adsorbents because of its ideal pore structure and many hydroxy groups on its surface.[21,22] However, the combination of manganese-based catalysts with CF and the influence of CF structure on the SCR reaction of the catalyst are not introduced in the research.

In present study, $MnO_x/\gamma\text{-}Al_2O_3$ was optimized by studying the loading number of active components and calcination temperature. The $MnO_x/\gamma\text{-}Al_2O_3$ catalyst ceramic filter (MA-CCF) was successfully synthesized by the one-step method. The MA-CCF was applied to the SCR of NO with NH_3. Compared with conventional $V_2O_5\text{-}WO_3/TiO_2$-based CCF, it maintained higher SCR activity over a wider temperature range. The effects of FV, H_2O, SO_2 and Na on NO conversion were investigated. Moreover, the mechanisms of reaction and poisoning were revealed by using XRD, SEM, BET, and XPS techniques. We hope the study can provide theoretical support for the development of potential, stable and more widely used catalytic ceramic filters.

2 Materials and methods

2.1 Preparation of manganese-based catalyst ceramic filter

The ceramic filter (CF) (JiangSu SaiTu New Material Technology Co., Ltd) was treated into a cylinder (L20 mm × Φ16 mm). After washing, acid treatment, and alkali treatment, it was dried at 100 °C and subsequently calcined at 400 °C for 3 h in a muffle furnace.

In this experiment, all the catalysts were prepared by the impregnation method. A certain amount of Mn $(CH_3COO)_2$-$\cdot 4H_2O$ (99.9%, Guang Fu, Tianjin, China) was measured and added to deionized water and stirred to form an aqueous solution. A certain amount of $\gamma\text{-}Al_2O_3$ (AR, Sinopharm Chemical Reagent, China) added in the solution. The mixture was stirred violently for 2 h and aged for 12 h at room temperature. After that, the immersion products were dried at 100 °C and calcined for 4 h. The as-catalyst was pressed and screened into granules (40–60 mesh). Catalyst samples were denoted as $xMnO_x/\gamma\text{-}Al_2O_3$ (MA), where x indicated x wt% of Mn in the catalyst.

The MA was loaded to the CF by a single-step coating method. Polyethylene glycol (PEG) was dissolved in distilled water, then added to the catalyst with a solid–liquid ratio of 20%, and stirred for 0.5 h. The pretreatment CF was placed in a beaker and sonicated for 5 min at 40 °C. After drying, it was recorded as a load once. Finally, the samples were calcined at 400 °C for 4 h, denoted as MA(y)-CCF, where y indicated the loading number of times with the catalyst. Simulated alkali metal poisoning was prepared by impregnation.

2.2 Sample characterization

X-ray diffraction (XRD) measurement was carried out on D/max 2500 V (Rigaku, Japan) using CuKα radiation, the diffraction angle (2θ) ranges from 5–75°. An automatic surface area and porosity analyzer (3H-2000PS2) was used to measure the N_2 adsorption isotherm and the specific surface area at 77 K. Pore volume and average pore diameter were obtained by the Barrett–Joyner–Halenda (BJH) method. The atomic valence content of the catalyst surface was determined by an X-ray Photoelectron Spectroscopy (XPS, Thermo, America). A new field-emission scanning electron microscopy (SEM, SU8032, Hitachi, Japan) was used to observe the sample microstructure with a voltage range of 0.1–30 kV.

2.3 Catalytic performance test

The loading rate (ω) is used to represent the coating firmness. ω is calculated according to the eqn (1):

$$\omega = \frac{m_1 - m_0}{m_1} \times 100\% \tag{1}$$

where m_0 is the quality of CF, and m_1 is the quality of MA(y)-CCF.

As shown in Fig. 1, the catalytic performance of the catalyst and the MA(y)-CCF were tested in the fixed-bed quartz reactor. The device comprised three units: gas distribution system, catalytic reaction system, and gas analysis system. The composition of the feed gas was as follows: 500 ppm NH_3, 500 ppm NO, 3 vol% O_2, 100 ppm SO_2 (when used), 10 vol% H_2O (when used), balanced with Ar. The total volume of gas in the catalyst activity measurement was 300 mL min^{-1} (GHSV = 35 000 h^{-1}). When MA(y)-CCF conducted the performance test, the gas volume was adjusted corresponding to the FV for 1 m min^{-1}. The gas analysis system was equipped with a portable gas analyzer to detect the flue gas composition. The NO conversion is calculated as:

$$NO_{conversion}(\%) = \frac{NO_{in} - NO_{out}}{NO_{in}} \times 100\% \tag{2}$$

3 Results and discussion

3.1 The optimal preparation of the MA(y)-CCF

3.1.1 The optimum preparation conditions of MA. The catalysts with different Mn loadings at the calcination temperature of 400 °C are shown in Fig. 2(a). The results presented that the highest NO conversion of $\gamma\text{-}Al_2O_3$ was only 24.2%. The catalytic efficiency was significantly improved with the loading of Mn. MnO_x enhanced the oxygen storage capacity of the catalyst and increased the concentration of chemisorbed oxygen on the surface.[23] At the same time, the multivalent Mn provided more acidic sites for the catalytic reaction.[24] The catalytic efficiency was increased with increasing Mn loading and reached its optimum when the loading reached 4 wt%. $4MnO_x/\gamma\text{-}Al_2O_3$ had the best activity and reached 100% NO conversion at 225–250 °C. And NO conversion was more than 90% at 150–350 °C. However, the denitration efficiency of the catalyst was decreased when Mn was added continuously. According to the monolayer dispersion theory, 5 wt% had exceeded $\gamma\text{-}Al_2O_3$ monolayer dispersion threshold, and MnO_x started to agglomerate, leading to a decrease in catalytic efficiency. Huang *et al.*[25] reached the same conclusion when $FeMnO_x$ was loaded on mesoporous silica (MPS). Finally, 4 wt% was chosen as the active component loading rate for the catalyst.
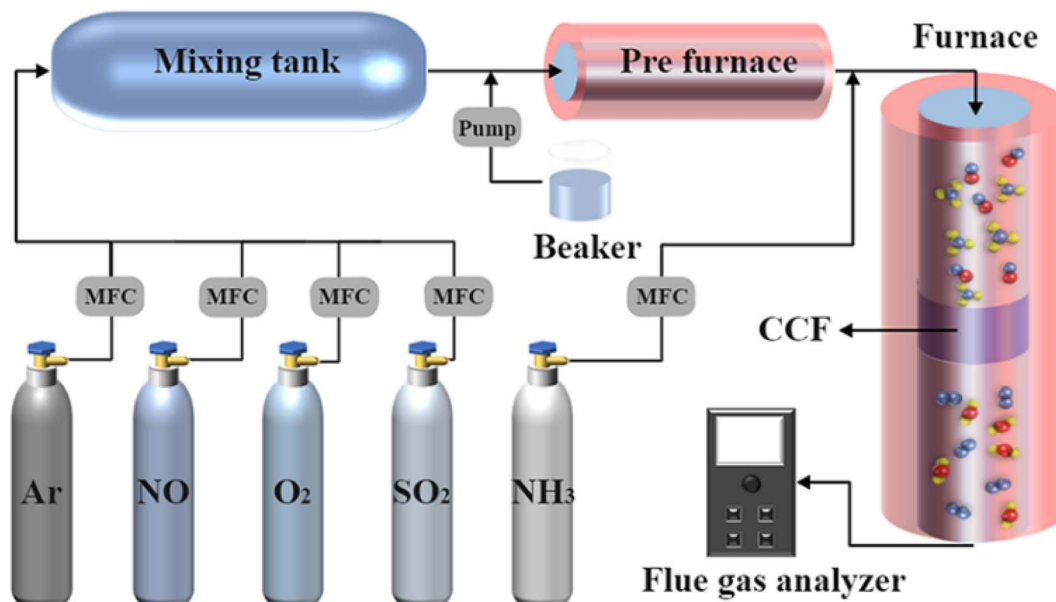
Fig. 1 Experimental device diagram.

The calcination temperature directly influences the catalyst's internal structure and the active component's dispersion in the support.[26] NO conversion of $4MnO_x/\gamma\text{-}Al_2O_3$ with different calcination temperatures is shown in Fig. 2(b). When the calcination temperature was 300 °C, the NO conversion was mainly reduced, probably due to the temperature being too low
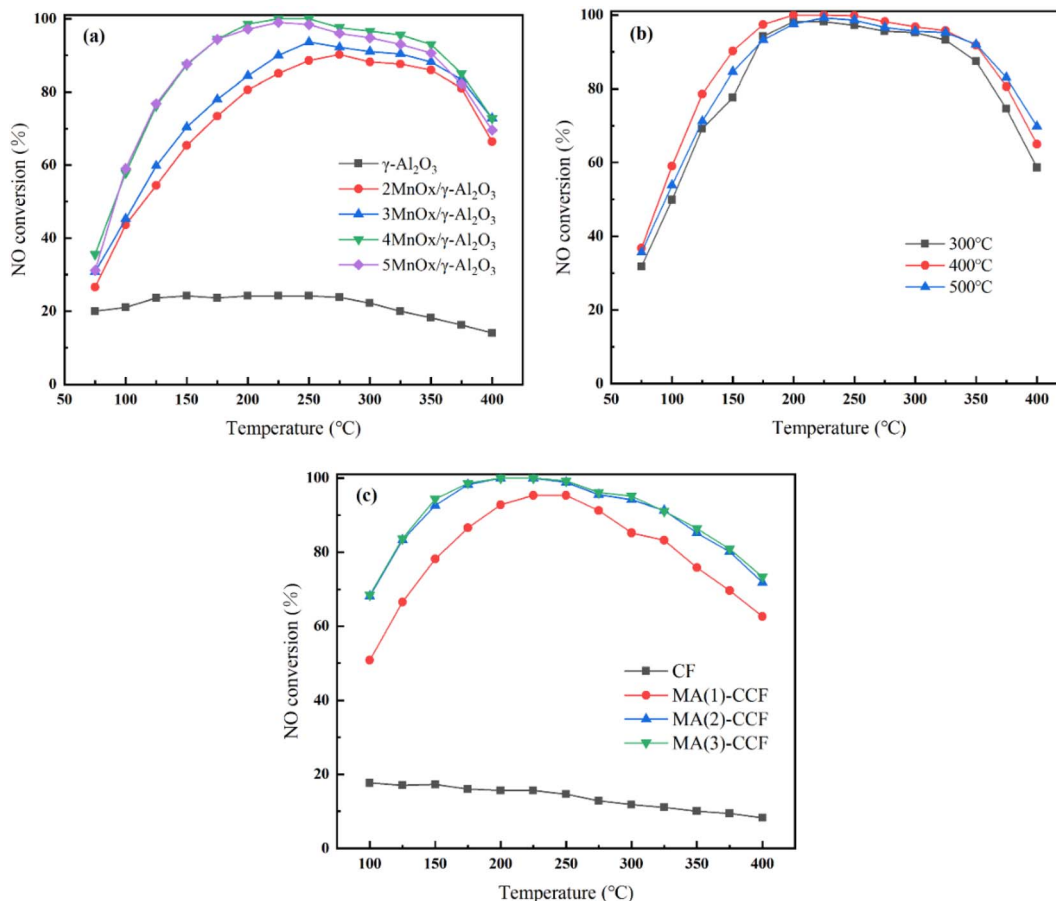

Fig. 2 NO conversion of (a) $\gamma\text{-}Al_2O_3$ and $xMnO_x/\gamma\text{-}Al_2O_3$ (b) $4MnO_x/\gamma\text{-}Al_2O_3$ with different calcination temperature (c) CF and MA(y)-CCF.

© 2023 The Author(s). Published by the Royal Society of Chemistry

Table 1 The influence of the loading number of times on the loading rate of MA(y)-CCF

Sample	MA(1)-CCF	MA(2)-CCF	MA(3)-CCF
The loading number of times	1	2	3
The loading rate(%)	9.7%	18.4%	20.1%

and the active component not completely decomposed.[27–29] When calcination was carried out 500 °C, the overall catalytic efficiency was decreased distinctly. Excessively high calcination temperatures could strengthen crystallinity of the catalyst.[30–32] Furthermore, the phenomenon of sintering and melting blocked the catalyst pore size and decreased specific surface area. It reduced the catalyst contact area with NO and the catalytic efficiency.[33,34] 400 °C was chosen as calcination temperature for the catalyst.

3.1.2 The optimum preparation conditions of the MA(y)-CCF. Table 1 shows the relationship between the loading number of times with $4MnO_x/\gamma\text{-}Al_2O_3$ and the loading rate of MA(y)-CCF. As the loading number of times with $4MnO_x/\gamma\text{-}Al_2O_3$ increased, the loading rate of MA(y)-CCF gradually increased. When the third load was finished, the pore area of the MA(3)-CCF decreased. However, the quality of the catalyst coating did not improve evidently when the number of loads was increased again.

The denitration efficiency of the blank CF was poor in Fig. 2(c). The highest NO conversion was only 17.6%. The NO conversion of MA(1)-CCF was 95.3% at 250 °C, and the NO conversion was >80% at 175–325 °C. Due to the increase in the catalyst loading, the denitration efficiency of the MA(2)-CCF significantly improved. It achieved 100% NO conversion at 200–250 °C, and NO conversion was above 80% at 125–375 °C. The denitration efficiency of MA(3)-CCF did not clearly improve compared with the second load. Considering the cost, MA(2)-CCF was selected for follow-up studies.

3.2 Characterization

3.2.1 XRD. Fig. 3 (a and b) shows the XRD patterns of $xMnO_x/\gamma\text{-}Al_2O_3$ with different active component loadings and different calcination temperatures. All samples contained diffraction peaks of $\gamma\text{-}Al_2O_3$, indicating that the support was not affected by the loading of the active component and maintained its original structure. $\gamma\text{-}Al_2O_3$ had high activity and large specific surface area.[35] MnO_x existed mainly in the form of $\beta\text{-}MnO_2$ and $\alpha\text{-}Mn_2O_3$. $\beta\text{-}MnO_2$ had stable structure, but SCR activity was poor.[36] A lot of activated oxygen vacancies and high N_2 selectivity of $\alpha\text{-}Mn_2O_3$ made it more SCR active.[37] None of the diffraction peaks of MnO_x were evident because of the excellent dispersion of MnO_x on the upper Al_2O_3 [25]. When the loading of Mn reached 4 wt% and the calcination temperature was 400 °C, the diffraction peaks of MnO_x become lower and broader, and the best dispersion was achieved. This provided more catalytic
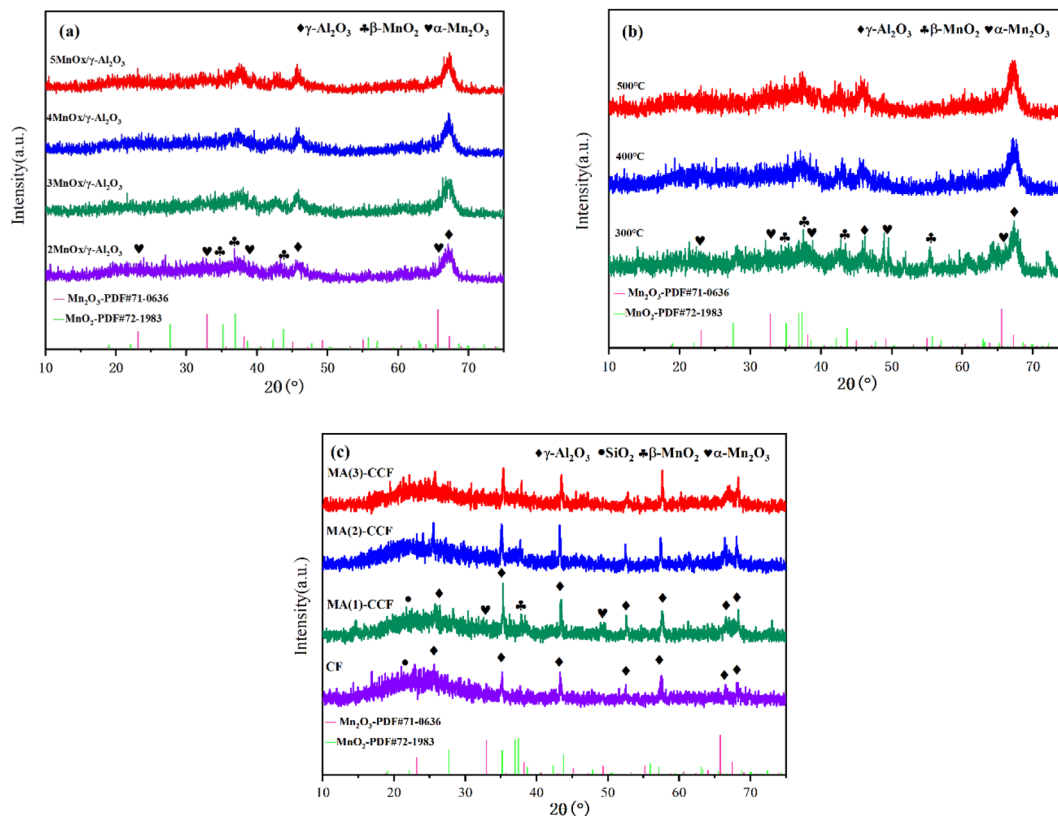

Fig. 3 XRD patterns of (a) $xMnO_x/\gamma\text{-}Al_2O_3$ (b) $4MnO_x/\gamma\text{-}Al_2O_3$ with different calcination temperature (c) CF and MA(y)-CCF.

Table 2 Mn2p, O1s binding energies of γ-Al$_2$O$_3$, 4MnO$_x$/γ-Al$_2$O$_3$ and the ratio of Mn^{4+}/(Mn^{4+} + Mn^{3+}) and O$_\alpha$/(O$_\alpha$ + O$_\beta$)

Test samples	Mn^{3+}	Mn^{4+}	Mn^{4+}/ (Mn^{4+} + Mn^{3+})	Binding energy at O$_\alpha$	Binding energy at O$_\beta$	O$_\alpha$/ (O$_\alpha$ + O$_\beta$)
γ-Al$_2$O$_3$	—	—	—	531.7	530.5	40.8%
4MnO$_x$/γ-Al$_2$O$_3$	642.0	643.3	57.1%	531.9	530.5	53.3%

active sites for the NH$_3$-SCR reaction and improved the catalytic activity and utilization of the catalyst. The XRD patterns of the MA(2)-CCF with different loadings showed the diffraction peaks of MnO$_x$, indicating the successful loading of the catalyst. The main composition of CF was α-Al$_2$O$_3$ and SiO$_2$. The activity of α-Al$_2$O$_3$ was low. But its strong crystalline and stable nature had made it widely used in industry.[35]

3.2.2 XPS. To further investigate the atomic components and elemental speciation on the catalyst surface, XPS characterizations of 4MnO$_x$/γ-Al$_2$O$_3$ and γ-Al$_2$O$_3$ were carried out, and the XPS spectra were fitted using XPS PEAK 4.1. By calculating the area, the proportion of each valence state of the elements was summarized in Table 2.

The Mn 2p XPS spectra of 4MnO$_x$/γ-Al$_2$O$_3$ in Fig. 4(a) included two characteristic peaks, Mn2p$_{1/2}$ and Mn2p$_{3/2}$. Combined with the XRD results, it could be concluded that MnO$_x$ was present in the prepared catalyst samples, and the valence of Mn was mainly +3 and +4. The Mn^{4+} concentration was 57.1%, indicating that the catalyst contained more MnO$_2$ than Mn$_2$O$_3$. The higher valence state of Mn^{4+} was more active for NH$_3$-SCR reaction than Mn^{3+} [38,39]. On the other hand, Mn^{3+} was more capable of promoting the conversion of NO to N$_2$.[40–42] Furthermore, each valence state's unbalanced content promoted oxygen vacancies on the catalyst surface,[43,44] further enhancing the catalyst's SCR activity.

The O 1s XPS spectra of 4MnO$_x$/γ-Al$_2$O$_3$ and γ-Al$_2$O$_3$ were implied in Fig. 4(b). The spectrum was fitted to two characteristic peaks, indicating that the sample contained two different kinds of oxygen species. The characteristic peaks between 528.9 eV and 530.8 eV at the binding energy corresponds to the lattice oxygen, O^{2-} (denoted as O$_\beta$) and the peaks between

530.8 eV and 533.33 eV at the binding energy corresponds to the surface chemisorbed adsorbed oxygen, O$^-$ (denoted as O$_\alpha$).[45–47] Surface-adsorbed oxygen was significantly more mobile than lattice oxygen.[48–50] It was also more reactive in SCR reaction and was quickly replenished from oxygen in the flue gas, making the surface-absorbed oxygen more conducive to the catalytic oxidation of NO$_x$.[40,51] The amount of surface-adsorbed oxygen and the proportion of adsorbed oxygen dissociating into active oxygen determined the catalyst activity,[52–54] so a higher O$_\alpha$ ratio represented higher catalyst oxidation activity.[55] The addition of the active component increased the O$_\alpha$/(O$_\alpha$ + O$_\beta$) ratio on the surface of the sample from 40.8% to 53.3% (Table 2), and MnO$_x$ enhanced the SCR activity of the catalyst.

3.2.3 SEM. To investigate the microscopic morphology of the CCF and the dispersion of the catalyst, SEM was carried out in combination with the EDS of each element distribution. From Fig. 5(a-1) and (a-2), the surface of the CF was a dense film composed of ceramic fibers, which provided the conditions for efficient dust filtration and catalyst loading. The EDS results presented that the elemental distribution of the ceramic fibers mainly contained Al, Si, and O, which was consistent with the XRD results (Fig. 5(a-3)). SEM of the CF after catalyst loading were implied in Fig. 5(b-1). The catalyst particles had not blocked the pore of the CF, and there was no evident agglomeration (Fig. 5(b-2)). The smaller catalyst particle size also helped expose the active catalytic sites and enhanced the catalytic performance of the CF. This could be concluded the one-step coating method for loading the catalyst onto CF was feasible. From Fig. 5(b-3), the uniform distribution of Mn indicated that the catalyst was uniformly distributed on the ceramic fibers.
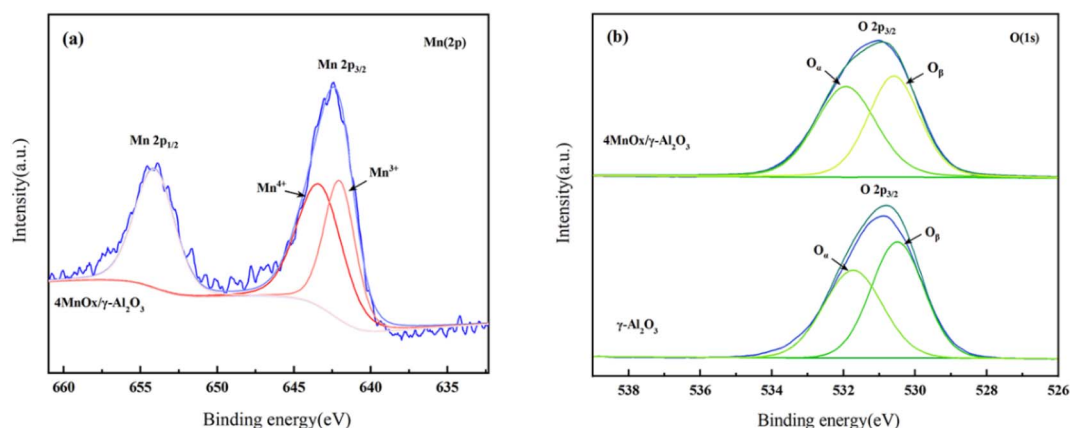
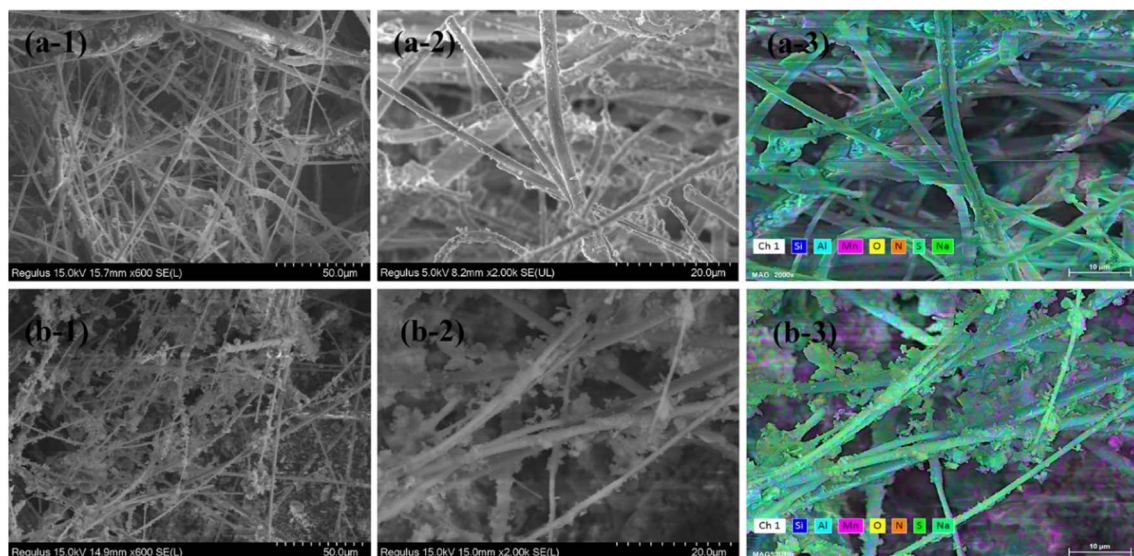**Fig. 4** XPS spectra of Al$_2$O$_3$, 4MnO$_x$/γ-Al$_2$O$_3$ (a) Mn2p (b) O1s.

Fig. 5   SEM results of CF and MA(2)-CCF.

3.2.4   BET. The specific surface area (S_{BET}) and pore structure of each sample are shown in Table 3. The N_2 sorption and desorption isotherms and pore size distribution are shown in Fig. 6. The catalyst and the CCF samples were both III isotherms with H3 hysteresis loop, indicating typical mesoporous characteristics. $4MnO_x/\gamma$-Al_2O_3 showed a large specific surface area (Fig. 6(a)). Generally, the larger the specific surface area of the catalyst could provide the more active sites, which was conducive to the adsorption and activation of the reactants.[56,57] The pore size of CF was mainly distributed between 10–40 nm (Fig. 6(b)). This indicated it had a dense internal structure with a high dust removal performance. Some pores of CF lay between 100 and 140 nm, which might be because some ceramic fibers were finer, resulting in larger pore sizes between the fibers. The pore size of $4MnO_x/\gamma$-Al_2O_3 was mainly distributed between 20–40 nm. After the catalyst loading, the pore size of MA(2)-CCF was decreased. But the specific surface area of MA(2)-CCF was increased, which provided more space for NH_3 and NO adsorption.[58] The increase in the pore volume of MA(2)-CCF was because some holes whose walls were destroyed become larger holes in the preparation process.

3.3   Catalytic activity test of the MA(2)-CCF

3.3.1   Effect of FV on the SCR catalytic activity. The CCF is a high-efficiency catalytic filter that integrates denitration and dust removal; hence, the FV is an essential factor affecting its use. From Fig. 7(a), when the FV was 0.6 m min^{-1}, the NO conversion of MA(2)-CCF exceeded 80% at 100–400 °C and reached 100% at 200–250 °C. When the FV increased to 1.4 m min^{-1}, the highest NO conversion was 95% at 200 °C and over 80% at 150–300 °C. Thus, MA(2)-CCF had excellent denitration performance at each FV.

3.3.2   Effect of SO_2 and H_2O on the SCR catalytic activity. In the flue gas of industrial furnaces, in addition to pollutants such as NO_x and dust, SO_2 and H_2O can affect the denitration activity of the CCF. Furthermore, the impact is more significant in the medium temperature section.[59] These observations mainly result from two aspects. H_2O can compete with NO and NH_3 in the gas for adsorption. The second is ammonium sulfate and ammonium sulfite generated by SO_2 and NH_3 do not reach the decomposition temperature (280 °C). This blocks the pores of the CF, resulting in a decrease in the specific surface area. Therefore, the experiment is carried out at the optimum temperature of 225 °C.

As shown in Fig. 7(b), when 100 ppm SO_2 was introduced, the NO conversion of MA(2)-CCF dropped slightly to 92.4%. Additionally, when the SO_2 supply was cut off, the NO conversion gradually recovered to 98.8%. When 10% H_2O was added to the reaction gas, the NO conversion first decreased and then increased. The NO conversion dropped as low as 91.8% and finally stabilized at about 95%. Compared with SO_2, adding H_2O had a more significant impact on the iteration efficiency in a short period. After cutting off the supply of H_2O, it recovered to 97.5%. Then, 100 ppm SO_2 and 10% H_2O were introduced,

Table 3   BET, pore volume, and average pore size of $4MnO_x/\gamma$-Al_2O_3, CF and MA(2)-CCF

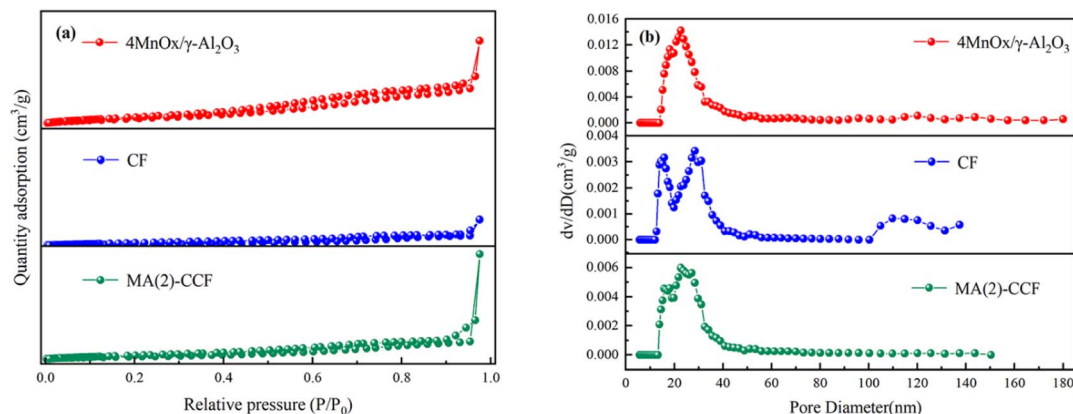| Sample	Specific surface area/(m^2 g^{-1})	Pore volume/(cm^3 g^{-1})	Average pore size/(nm)
$4MnO_x/\gamma$-Al_2O_3	109.03	0.51	9.41
CF	17.21	0.16	1.80
MA(2)-CCF	52.81	0.65	2.45

Fig. 6 N$_2$ absorption and desorption curves and pore size distribution of 4MnO$_x$/γ-Al$_2$O$_3$, CF and MA(2)-CCF.

and the NO conversion of MA(2)-CCF gradually decreased and stabilized at about 88%. When the supply of the two components was cut off, the NO conversion gradually recovered to 93.6%. Therefore, MA(2)-CCF had good water and sulfur tolerance.

After the sulfur resistance experiment, the characteristic peak of MnO$_x$ on the surface of the MA(2)-CCF become weaker (Fig. 7(c)), indicating that MnO$_x$ and SO$_2$ might have formed

Mn(SO$_4$)$_2$.[60–62] The specific surface area and average pore size were reduced, and the number of pores around 15 nm was increased (Fig. 7(d)), we hypothesized that the generated Mn(SO$_4$)$_2$, NH$_4$(SO$_4$)$_2$, and NH$_4$HSO$_2$ blocked the large pores.[63–65] However, the change in the characteristic peak of MnO$_x$ inside MA(2)-CCF was small. There was no apparent change in the pore size between fibers, which indicated the dense membrane and high-density fiber on the outer layer of
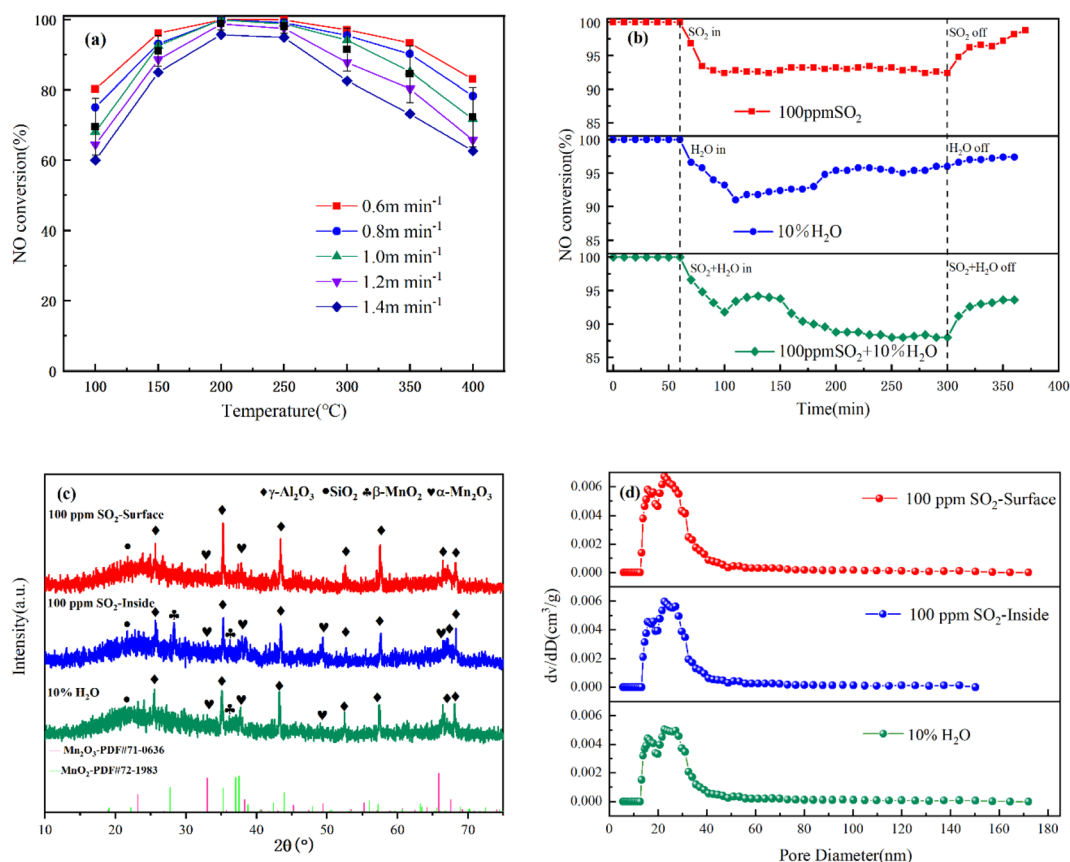

Fig. 7 (a) NO conversion of MA(2)-CCF with different FV (b) NO conversion (c) XRD spectrum (d) pore size distribution of MA(2)-CCF in the presence of SO$_2$ and H$_2$O at 225 °C.

the CF could effectively protect the catalyst loaded inside it and reduce the influence of SO_2 on the catalyst.

After the water resistance experiment, the XRD result of MA(2)-CCF was poisoned by H_2O was not much different from MA(2)-CCF, indicating that H_2O did not destroy the material composition of the CCF. The effect of H_2O on denitration efficiency was mainly in two aspects. First, in a high-temperature environment, high-temperature water vapor could destroy the support structure.[66] BET results in Fig. 7(d) showed that the specific surface area of the MA(2)-CCF after 10% H_2O decreased and average pore size increased, indicating that the high-temperature water vapor damaged the structure of the MA(2)-CCF. Additionally, it led to catalyst agglomeration, reducing the contact area between the catalyst and the airflow, and reducing the catalyst utilization rate.

Secondly, the catalyst adsorbed H_2O to form surface –OH, which covered the surface-active sites, hindered the adsorption of NH_3 and NO, and reduced the catalytic efficiency of the catalyst.[67,68] However, in a higher-temperature environment, –OH desorption was also faster. When the effect of structural damage dropped to the threshold, the –OH desorption weakened the inhibitory effect of H_2O. The rebound of NO conversion was consistent with the experimental result.

3.3.3 Effect of Na on the SCR catalytic activity. The alkali metals produced by burning coal are mainly Na. Some industrial production processes, such as glass, add sodium salt as a clarifying agent. The desulfurization treatment before the SCR process often uses a sodium-based desulfurizer. The alkali metal in the flue gas can deposit on the catalyst and cause alkali poisoning, occupy the acid sites on the surface, and inhibit the reaction of the active site, which seriously affects the denitration activity of the catalyst.[69,70]

The denitration efficiency of MA(2)-CCF was significantly reduced after Na poisoning (Fig. 8(a)). 225 °C was found to be the optimum temperature for denitration activity of MA(2)-CCF. When Na was 1% of the weight of the catalyst, the NO conversion dropped to 83%. However, when the mass fraction of Na was increased, the NO conversion of MA(2)-CCF did not decrease sufficiently.

There was no diffraction peak of Na in MA(2)-CCF after Na poisoning, which might be due to the low content of Na_2O or the existence of an amorphous form (Fig. 8(b)). After alkali poisoning, the denitration performance of the CCF was decreased. However, the specific surface area increased, indicating that the specific surface area was not the only factor affecting alkali metals' denitration efficiency. Wang et al.[71] modified $V_2O_5–WO_3/TiO_2$ with Nb and BET analysis and verified this result. The decrease in pore volume and average pore size and the increase in the number of pores between 10 and 20 nm in the pore size distribution were shown in Fig. 8(c). It
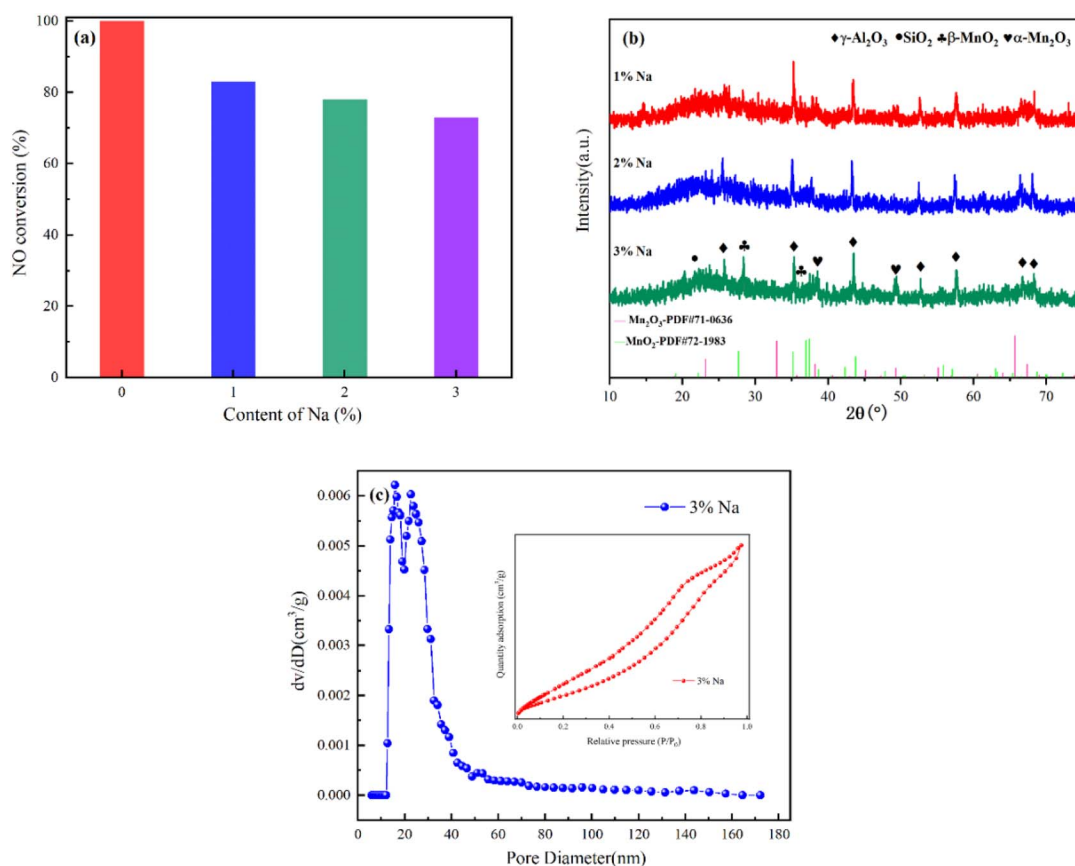

Fig. 8 (a) NO conversion (b) XRD spectrum (c) N_2 absorption and desorption curves and pore size distribution of MA(2)-CCF are poisoned by Na at 225 °C.
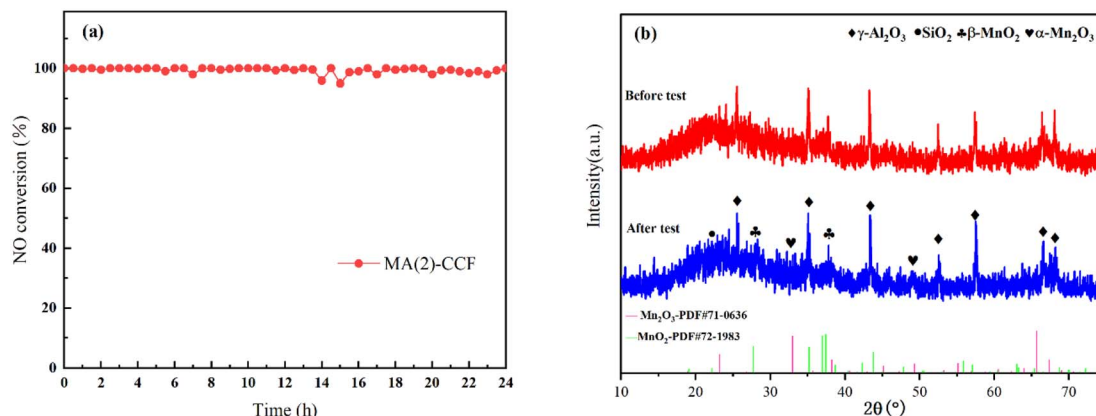
Fig. 9 (a) Stability test of MA (2)-CCF at 225 °C(b) XRD spectrum of MA(2)-CCF before and after stability test.

proved one of the ways that alkali metals poison the catalyst was by blocking the pore size and loading the catalyst to reduce active surface sites and reduce its denitration performance.[72-75]

3.3.4   Stability test. The stability of denitration is a very important factor affecting industrial applications. MA(2)-CCF was chosen for further study into its stability and the result was shown in Fig. 9(a). The denitration efficiency fluctuated slightly within 14–15 h, but the change was not significant. Overall, MA(2)-CCF has good stability for 24 h operation in the SCR reaction. XRD patterns of MA(2)-CCF before and after the 24 h reaction were found no change (Fig. 9(b)). It further explained that MA(2)-CCF had the potential for industrial application.

4   Conclusions

(1) MnO_x/Al_2O_3 was prepared by an impregnation method. The dispersion of active components was also an essential factor affecting the denitration activity of the catalyst. When the loading amount was 4 wt% and the calcination temperature was 400 °C, the NO conversion was more than 90% at 150–350 °C. In addition, we will continue to study the N_2 selectivity of MnO_x/Al_2O_3 and further explore its SCR reaction mechanism in the future.

(2) Under the FV of 1 m min^{-1}, the NO conversion of MA(2)-CCF was above 80% at 125–375 °C. Water and sulfur tolerance of it were better and it showed good tolerance to alkali metal poisoning at 225 °C. MA(2)-CCF had good stability for 24 h at 225 °C.

(3) According to XRD, SEM, and BET results, there were two reasons for SO_2 poisoning in the MA(2)-CCF. One was that the ammonium sulfate generated by SO_2 and NH_3 deposits on the surface of the MA(2)-CCF. The second was that the sulfate generated by the catalyst reduced the number of active sites. The influence of H_2O mainly lay in the destruction of the fiber structure of the MA(2)-CCF. Alkali metal poisoning occurred due to the deposition of oxide generated by the alkali metal. It blocked the pore channel and covered the catalyst loaded on the surface of the MA(2)-CCF. The dense surface film and unique

ceramic fiber structure of MA(2)-CCF could effectively protect the internal catalyst and reduce the poisoning effect, which had a high industrial application prospect.

Author contributions

Zhenzhen Wang: writing – investigation, original draft, methodology, date curation, formal analysis, software. Shuchuan Peng: supervision, validation. Chengzhu Zhu: methodology, writing – review & editing. Bin Wang: resources, project administration. Bo Du: formal analysis. Ting Cheng: formal analysis. Zhaozhong Jiang: formal analysis. Lei Sun: conceptualization, supervision, funding acquisition, visualization.

Conflicts of interest

The authors declared that they have no conflicts of interest to this work.

Acknowledgements

References

1 H. Lin, A. Abubakar, C. Li, Y. Li, C. Wang, S. Gao, Z. Liu and J. Yu, *Catal. Lett.*, 2019, **150**, 702–712.

2 J. Yu, C. Li, F. Guo, S. Gao, Z.-G. Zhang, K. Matsuoka and G. Xu, *Fuel*, 2018, **219**, 37–49.

3 L. Guo, J. Lu, Y. Zhao, C. Wang, C. Zhang, C. Tang, L. Dong, W. Kong, Q. Li and P. Cao, *Catal. Sci. Technol.*, 2021, **11**, 3164–3175.

4 X. Liu, C. A. Wang, T. Zhu, Q. Lv, Y. Li and D. Che, *Chem. Eng. J.*, 2019, **371**, 486–499.

5   R. Xiao, T. Gao, X. Cui, Y. Ji, Y. Zhang, X. Chuai, Z. Xiong, Y. Liao, H. Gu, J. Yang, J. Zhang and Y. Zhao, *Fuel*, 2022, **310**, 122219.

6   J.-H. Choi, J.-H. Kim, Y.-C. Bak, R. Amal and J. Scott, *Korean J. Chem. Eng.*, 2005, **22**, 844–851.

7   J.-H. Choi, S.-K. Kim, S.-J. Ha and Y.-O. Park, *Korean J. Chem. Eng.*, 2001, **18**, 456–462.

8   J.-H. Choi, S.-K. Kim and Y.-C. Bak, *Korean J. Chem. Eng.*, 2001, **18**, 719–724.

9   S. Heidenreich, M. Nacken, M. Hackel and G. Schaub, *Powder Technol.*, 2008, **180**, 86–90.

10 M. Nacken, S. Heidenreich, M. Hackel and G. Schaub, *Appl. Catal., B*, 2007, **70**, 370–376.

11 Z. An, G. Niu, Z. Tan, T. Shang and X. Yang, *Therm. Power. Gen.*, 2017, **46**, 36–41.

12 C. Yu, *Master*, XiangTan University, 2018.

13 Y. Zhang, C. Li, C. Yu, T. Tran, F. Guo, Y. Yang, J. Yu and G. Xu, *Chem. Eng. J.*, 2017, **330**, 1082–1090.

14 Y.-S. Zhang, C. Li, C. Wang, J. Yu, G. Xu, Z.-g. Zhang and Y. Yang, *Ind. Eng. Chem. Res.*, 2019, **58**, 828–835.

15 J. Svachula, N. Ferlazzo, P. Forzatti, E. Tronconi and F. Bregani, *Ind. Eng. Chem. Res.*, 1993, **32**, 1053–1060.

16 C. Wang, C. Li, Y. Li, L. Huangfu, Z. Liu, S. Gao and J. Yu, *Ind. Eng. Chem. Res.*, 2019, **58**, 19847–19854.

17 J. Xiang, L. Wang, F. Cao, K. Qian, S. Su, S. Hu, Y. Wang and L. Liu, *Chem. Eng. J.*, 2016, **302**, 570–576.

18 G. Zhai, Z. Han, X. Wu, H. Du, Y. Gao, S. Yang, L. Song, J. Dong and X. Pan, *J. Taiwan Inst. Chem. Eng.*, 2021, **125**, 132–140.

19 H. Zhou, L. Qian, T. Cheng, B. Du, F. Xia and C. Zhu, *J. Chem.*, 2022, **2022**, 5049161.

20 T. Wang, C. Zhu, H. Liu, Y. Xu, X. Zou, B. Xu and T. Chen, *Environ. Technol.*, 2017, **42**, 2705–2715.

21 L. Han, M. Gao, C. Feng, L. Shi and D. Zhang, *Environ. Sci. Technol.*, 2019, **53**, 5946–5956.

22 Z. Fan, J.-W. Shi, C. Niu, B. Wang, C. He and Y. Cheng, *Chem. Eng. J.*, 2020, **398**, 125572.

23 T. Qiao, Z. Liu, C. Liu, W. Meng, H. Sun and Y. Lu, *Appl. Catal., A*, 2021, **617**, 118128.

24 Z. Fan, J.-W. Shi, C. Gao, G. Gao, B. Wang, Y. Wang, C. He and C. Niu, *Chem. Eng. J.*, 2018, **348**, 820–830.

25 J. Huang, Z. Tong, Y. Huang and J. Zhang, *Appl. Catal., B*, 2008, **78**, 309–314.

26 L. Xu, S. Niu, C. Lu, Q. Zhang and J. Li, *Fuel*, 2018, **219**, 248–258.

27 H. Xu, M. Sun, S. Liu, Y. Li, J. Wang and Y. Chen, *RSC Adv.*, 2017, **7**, 24177–24187.

28 Z. Han, Q. Yu, Z. Teng, B. Wu, Z. Xue and Q. Qin, *Environ. Sci. Pollut. Res.*, 2019, **26**, 12920–12927.

29 S. M. Lee, H. H. Lee and S. C. Hong, *Appl. Catal., A*, 2014, **470**, 189–198.

30 Y. Yu, J. Zhang, C. Chen, C. He, J. Miao, H. Li and J. Chen, *J. Environ. Sci.*, 2020, **91**, 237–245.

31 L. Ma, J. Li, H. Arandiyan, W. Shi, C. Liu and L. Fu, *Catal. Today*, 2011, **184**, 145–152.

32 Z. Song, Z. Huang, B. Liu, H. Liu, X. Zhu, F. Xia, H. Kang, Y. Mao, X. Liu, B. Zhao and Q. Zhang, *Microporous Mesoporous Mater.*, 2019, **292**, 109753.

33 Q. Liu, C. Bian, Y. Jin, L. Pang, Z. Chen and T. Li, *Catal. Today*, 2022, **388–389**, 158–167.

34 L. Jia, J. Liu, D. Huang, J. Zhao, J. Zhang, K. Li, Z. Li, W. Zhu, Z. Zhao and J. Liu, *ACS Catal.*, 2022, **12**, 11281–11293.

35 J. Zhang, Y. Li, L. Wang, C. Zhang and H. He, *Catal. Sci. Technol.*, 2015, **5**, 2305–2313.

36 J. Liu, Y. Wei, P. Li, P. Zhang, W. Su, Y. Sun, R. Zou and Y. Zhao, *ACS Catal.*, 2018, **8**, 3863–3874.

37 S. Mo, Q. Zhang, J. Li, Y. Sun, Q. Ren, S. Zou, Q. Zhang, J. Lu, M. Fu, D. Mo, J. Wu, H. Huang and D. Ye, *Appl. Catal., B*, 2019, **264**, 118646.

38 S. Zhang, Y. Zhao, J. Yang, J. Zhang and C. Zheng, *Chem. Eng. J.*, 2018, **348**, 618–629.

39 Q. Xu, Z. Fang, Y. Chen, Y. Guo, Y. Guo, L. Wang, Y. Wang, J. Zhang and W. Zhan, *Environ. Sci. Technol.*, 2020, **54**, 2530–2538.

40 G. Zhai, J. Wang, Z. Chen, S. Yang and Y. Men, *J. Hazard. Mater.*, 2019, **363**, 214–226.

41 G. Zhai, J. Wang, Z. Chen, W. An and Y. Men, *Chem. Eng. J.*, 2018, **337**, 488–498.

42 J. Wang, C. Zhang, S. Yang, H. Liang and Y. Men, *Catal. Sci. Technol.*, 2019, **9**, 6379–6390.

43 C. Liu, F. Li, J. Wu, X. Hou, W. Huang, Y. Zhang and X. Yang, *J. Hazard. Mater.*, 2019, **363**, 439–446.

44 C. Niu, B. Wang, Y. Xing, W. Su, C. He, L. Xiao, Y. Xu, S. Zhao, Y. Cheng and J.-W. Shi, *J. Cleaner Prod.*, 2021, **290**, 125858.

45 L. Yao, Q. Liu, S. Mossin, D. Nielsen, M. Kong, L. Jiang, J. Yang, S. Ren and J. Wen, *J. Hazard. Mater.*, 2020, **387**, 121704.

46 M. Salazar, S. Hoffmann, L. Tillmann, V. Singer, R. Becker and W. Grünert, *Appl. Catal., B*, 2017, **218**, 793–802.

47 D. Fang, J. Xie, H. Hu, H. Yang, F. He and Z. Fu, *Chem. Eng. J.*, 2015, **271**, 23–30.

48 R. Luo, Y. Zeng, S. Ju, S. Feng, F. Zhang, Z. Zhong and W. Xing, *Ind. Eng. Chem. Res.*, 2022, **61**, 5816–5824.

49 F. A. Deorsola, S. Andreoli, M. Armandi, B. Bonelli and R. Pirone, *Appl. Catal., A*, 2016, **522**, 120–129.

50 L. Wang, B. Huang, Y. Su, G. Zhou, K. Wang, H. Luo and D. Ye, *Chem. Eng. J.*, 2012, **192**, 232–241.

51 L. Cheng, J. Wang, C. Zhang, B. Jin and Y. Men, *New J. Chem.*, 2019, **43**, 19126–19136.

52 Z. Zhang, J. Li, J. Tian, Y. Zhong, Z. Zou, R. Dong, S. Gao, W. Xu and D. Tan, *Fuel Process. Technol.*, 2022, **230**, 107213.

53 S. S. R. Putluru, L. Schill, A. D. Jensen, B. Siret, F. Tabaries and R. Fehrmann, *Catalysts*, 2021, **22**, 259.

54 D. Meng, Q. Xu, Y. Jiao, Y. Guo, Y. Guo, L. Wang, G. Lu and W. Zhan, *Appl. Catal., B*, 2018, **221**, 652–663.

55 J. Liu, M. Jing, R. Tao, W. Song, H. Cheng, H. Li, Z. Zhao, J. Liu, W. Zhu and S. Dai, *Fuel*, 2023, **333**, 126303.

56 A. Xie, Y. Tao, X. Jin, P. Gu, X. Huang, X. Zhou, S. Luo, C. Yao and X. Li, *New J. Chem.*, 2019, **43**, 2490–2500.

57 J. Liu, H. Cheng, H. Zheng, L. Zhang, B. Liu, W. Song, J. Liu, W. Zhu, H. Li and Z. Zhao, *ACS Catal.*, 2021, **11**, 14727–14739.

58 Y. Li, Z. liu, X. Li and Y. Hou, *Mol. Catal.*, 2021, **509**, 111635.

59 R. Wang, L. Zhao, X. Hu, Z. Liu, H. Zhang and J. Jin, *Mater. Res. Express*, 2019, **6**, 115512.

60 Z. L. Guan J, W. Li, D. Hu, J. Wen and B. Huang, *Catalysts*, 2021, **11**, 324.

61 Q. Wang, R. Wang, X. Huang and H. Shi, *J. Environ. Chem. Eng.*, 2022, **10**, 107345.

62 J. Wang, X. Yi, Q. Su, J. Chen and Z. Xie, *Catal. Sci. Technol.*, 2021, **11**, 2852–2863.

63 C. Gao, J.-W. Shi, Z. Fan, B. Wang, Y. Wang, C. He, X. Wang, J. Li and C. Niu, *Appl. Catal., A*, 2018, **564**, 102–112.

64 X. Wu, Q. Shi, Y. Xu, J. Wang and X. Zhang, *Appl. Clay Sci.*, 2020, **185**, 105200.

65 S. Pan, H. Luo, L. Li, Z. Wei and B. Huang, *J. Mol. Catal. A: Chem.*, 2013, **377**, 154–161.

66 Y. Li, X. Han, Y. Hou, Y. Guo, Y. Liu, Y. Cui and Z. Huang, *Chem. Eng. J.*, 2018, **347**, 313–321.

67 B. Zhang, M. Liebau, W. Suprun, B. Liu, S. Zhang and R. Gläser, *Catal. Sci. Technol.*, 2019, **9**, 4759–4770.

68 K. Liu, Z. Yan, H. He, Q. Feng and W. Shan, *Catal. Sci. Technol.*, 2019, **9**, 5593–5604.

69 M. Kong, Q. Liu, J. Zhou, L. Jiang, Y. Tian, J. Yang, S. Ren and J. Li, *Chem. Eng. J.*, 2018, **348**, 637–643.

70 L. Liu, X. Wu, Y. Ma, X. Zhang, R. Ran, Z. Si and D. Weng, *Chem. Eng. J.*, 2020, **383**, 123080.

71 B. Wang, Y. Bian, Q. Feng, S. Wang and B. Shen, *J. Fuel Chem. Technol.*, 2022, **50**, 503–512.

72 P. Wu, K. Shen, Y. Liu, Y. Zhang, G. Li, H. Yang and S. Wang, *Catal. Sci. Technol.*, 2021, **11**, 4115–4132.

73 B. Zhu, Z. Zi, Y. Sun, Q. Fang, J. Xu, W. Song, H. Yu and E. Liu, *Catal. Sci. Technol.*, 2019, **9**, 3214–3225.

74 L. Lisi, G. Lasorella, S. Malloggi and G. Russo, *Appl. Catal., B*, 2004, **50**, 251–258.

75 P. Wu, X. Tang, Z. He, Y. Liu and Z. Wang, *Energy Fuels*, 2022, **36**, 5622–5646.